Large Scale Terahertz Sensor Array Module with Antenna Coupled Microbolometers on Glass Substrate with Sigma Delta ADC Readout ASIC

John Hong, *Senior Member, IEEE*, Sean Andrews, Jan Bos, Edward Chan, Tallis Chang, Vincent Condito *Member, IEEE*, Alan Lewis, *Fellow*, *IEEE*, Murilo Pessatti *Member, IEEE,* Seung Tak Ryu *Senior Member, IEEE*, Heesun Shin, and Bing Wen

***Abstract*— We describe the design, fabrication and demonstration of a terahertz sensor array module, designed to operate over 250-350GHz. The antenna coupled microbolometer was fabricated on a glass substrate with an integrated array of pixel switches and row multiplexing circuitry implemented with LTPS (Low Temperature PolySilicon) thin film transistors. While other microbolometer arrays have been reported for the upper Terahertz bands, we focus on lower frequencies where adequate semiconductor sources are available potentially enabling important medical and security applications. The devices were fabricated in a Gen 3.5 flat panel manufacturing facility implementing what we call Large Area MEMS Platform (LAMP) surface micromachining process, providing a path to low-cost manufacturing. Individual pixels were defined on a 0.7mm pitch across an array of 128x128 pixels in this first demonstration. Since flat panel fabrication capabilities use large, single-shot reticle masks and large glass substrates, physically larger arrays can be manufactured without mask stitching. An ROIC (readout integrated circuit) was demonstrated to support the THz sensor panel with 648 input channels, each providing an independent sigma delta ADC with excellent uniformity and 12 effective number of bits. An early demonstration of the sensor array is described, imaging a metallic knife hidden in a cardboard envelope.**

***Index Terms*—Camera, Microbolometer, Terahertz, Large Pixels, Array**

I. INTRODUCTION

Imaging across the terahertz spectrum has been shown to be exceptionally effective in a number of important applications [1-12]. The excellent reviews by Siegel [13] and Mittleman [14] sketch the impressively broad landscape of potential uses as well as the state of the art in the technology progress to date. Ambitious systems have been demonstrated for applications such as concealed weapons screening [15-18], manufacturing quality inspections [19] and medical imaging [20-25]. Applications in the lower THz frequencies are especially intriguing such as the use of THz reflective imaging to distinguish diseased from normal tissue, such as the experiments performed by the Yonsei University group [26] who investigated its use in detecting and quantifying the margins of glioblastoma tumors in mouse brains. In that experiment, a single pixel detector was scanned to produce startling images that competed favorably with fluorescence imaging that relies on the use of expensive prodrugs such as 5-ALA [27]. In the THz case, the difference in local water content provides the imaging contrast without reliance on externally injected chemicals. While scanned images can be useful in pathology and research settings, a staring camera that can produce such images at video frame rates (30Hz) could become an important instrument in surgical and other environments to help make real time decisions. In both medical imaging and security screening applications, the lower frequency region of the THz spectrum, namely in the neighborhood of 300GHz, is especially useful as the radiation is sensitive to water absorption and also allows for a degree of penetration into tissue for the medical application and through clothes for usage in security screening.

Building a THz imaging camera requires an illumination source, a lens, and an imaging sensor array. Diode multipliers and III-V transistor based amplifiers have matured to enable a variety of commercial products that can source milliwatts of power in the neighborhood of 300GHz [28]. Low-loss lens materials such as high-density polyethylene (HDPE) are readily available and can be machined using CNC to the proper tolerances for good optical performance [29]. In this paper, we focus on the design and demonstration of a large sensor array that can be integrated with the aforementioned components to realize a complete, reflective imaging system.

The long wavelength of 300GHz radiation poses a unique challenge, since the pixel pitch is proportional to the wavelength, and arrays that are designed for higher frequencies will be oversampling the image plane far above the required Nyquist rate while severely restricting the field of view. A diffraction limited lens with circular aperture has a modulation transfer function (MTF) that is bandlimited to $1/(\lambda F\#)$ where F# is the focal ratio given by the focal length divided by the lens diameter. Nyquist sampling requires a minimum sampling

John Hong is with Obsidian Sensors, San Diego, CA 92122 USA (e-mail: john.hong@obsidiansensors.com) and also UCSD ECE Department, La Jolla, CA 92093.

Sean Andrews, Jan Bos, Edward Chan, Tallis Chang, Vincent Condito, Alan Lewis, Heesun Shin, and Bing Wen are all with Obsidian Sensors, San Diego, CA 92122.

Murilo Pessatti is with Chipus Microelectronics in Florianopolis, Santa Catarina, Brazil.

Seung-Tak Ryu is with Korea Advanced Institute of Science and Technology in Daejon, South Korea.

This material is based upon work partially supported by the U. S. National Science Foundation under Grant No. 2013992. Any opinions, findings, and conclusions or recommendations expressed in this material are those of the author(s) and do not necessarily reflect the views of the National Science Foundation.

frequency of twice that bandlimit, resulting in a pitch of (λF#)/2 which is 0.7mm at 300GHz for F#=1.4. A 128x128 array would therefore have an active area bounded by 90mm x 90mm which enables a large real time field of view that is otherwise unattainable in other technologies. In addition, the large pixels are designed for high sensitivity (minimum detectable power, MDP, less than 60 pW/pixel) yet maintain the speed required to operate at over 30 frames per second. For comparison, THz cameras summarized in Table 3 that have reported impressive performance metrics have either very few pixels or used pixel pitches that range from 25um to 50um [30-36, 41-42] which are at least an order of magnitude smaller than what is required for operation at 300GHz with a reasonable field of view. Proper scaling of pixels given the frequency of operation and the camera optics has been addressed in a recent survey of THz cameras by Oda [32]. A wide variety of sensor technologies are reviewed in that paper. Some of the references are summarized in Table 1. We report here our development and results of a THz antenna-coupled, uncooled microbolometer array, monolithically fabricated on a large glass substrate with its own readout integrated circuit (ROIC). In what follows, we discuss the design aspects of the project along with demonstrations of the operation of the sensor array in a simple shadow casting experiment. Fabrication challenges reduced the measured pixel sensitivity. We also describe in some detail, the design and demonstration of the ROIC built specifically for the system.

II. Sensor Array Panel

A. Module Design

The envisioned module starts with a sensor array panel to be implemented using a MEMS on Glass fabrication platform that integrates surface micromachined structures on top of display grade thin film transistor (TFT) electronics. We successfully set up a fabrication process at a leading display production company using LTPS (low temperature polysilicon) provisioning the TFT function. The process layer construction is shown schematically in Figure 1. The MEMS layers are composed of metal/dielectrics/semiconductor materials commonly available in LCD TFT fabs and use a polyimide material for the sacrificial layer. LTPS can be NMOS, PMOS or CMOS.

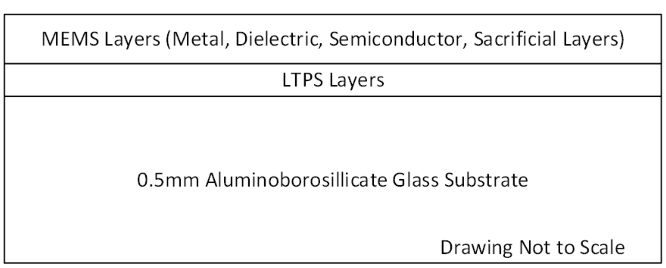

Fig. 1. MEMS on LTPS Glass Layer Construction

The LTPS transistor layer provisions a matrix of pixel switches that enable sequential row addressing scheme common to most display devices today. The module architecture is illustrated in Figure 2, showing the sensor panel (with integrated row multiplexer) and the ROIC as two constituent components. The sensing element is a microbolometer whose construction is described in more detail later. Briefly, it is an antenna-coupled bolometer whose temperature dependent resistance is read out by applying a voltage bias and selecting the row to connect to a column read line. The ROIC reads out the current in the column line and digitizes it. As discussed earlier, the array geometry, namely the pixel pitch, is determined by the wavelength of operation, in most imaging systems. For the nominal 300GHz operation, we choose a pitch of 0.7mm. Herein is the key advantage of our design/fabrication approach. The MEMS on glass fabrication process is built on a Gen 3.5 glass substrate which measures 620mm x 750mm. Mask steppers built for the flat panel industry typically operate with a 6”x6” reticle so that arrays larger than 300x300 are possible without stitching, and each substrate can yield many devices whose individual size approaches that of a 200mm Si wafer. The limitation of the 200mm wafer size may be the reason why previous THz cameras operate with much smaller pitch (typically 30-50um) or have fewer pixels than our system. To our knowledge, the largest pixels reported to date are a 31x31 array with 240x240um^2 pixels for operation at 270GHz [41] and the Tera-4096 64x64 array with 1.5x1.5mm^2 pixels [34]. The custom ROIC designed and fabricated for the THz application provides up to 648 input channels, each with a second order sigma delta analog to digital converter, along with clock generation and programmable FIR filter coefficients to optimize the conversion process. The ROIC is bonded onto the glass panel using a standard chip on glass (COG) process commonly used in the display industry.

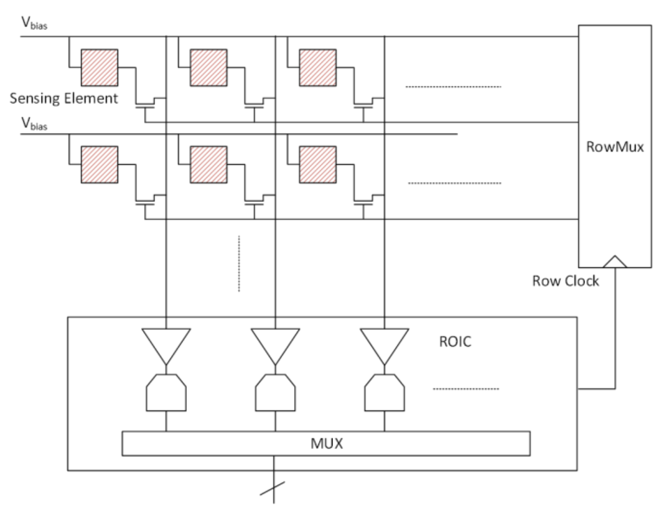

Fig. 2. THz Sensing Array Module Architecture

The device that we were able to fabricate is shown in Figure 3, based on the design that will be discussed in the next section. In what follows, we give more detailed descriptions of the sensor panel design and the ROIC that was designed for the THz application and conclude with a simple demonstration of the module.

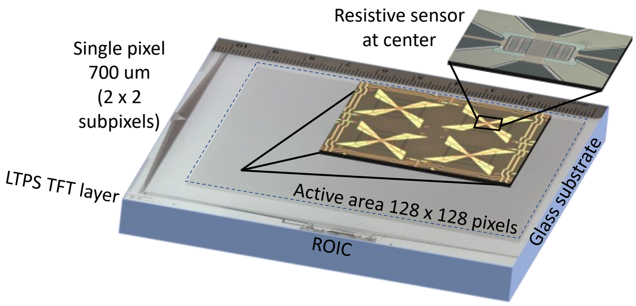

Fig. 3. Actual Sensor Module 128x128

B. Pixel Design

The array design targeted a 0.7mm pitch, 128x128 pixel format, antenna coupled microbolometer construction. As shown in Figure 4, the antenna elements are coupled capacitively through air gaps to the bolometric sensor which itself must be suspended above the substrate to provide adequate thermal isolation. Radiation enters the pixel through the substrate glass and induces currents in the crossed-dipole antenna elements. The dipoles have gaps at the center which force the current to couple capacitively to the Titanium Nitride load which is shaped as a cross that is separated from the antenna metal by a 3 um gap. The Titanium Nitride has a thickness and resistivity tailored to produce a real resistance of 500 ohms. This value which is close but not exactly equal to the free space wave impedance of 377 Ohms, was optimized in COMSOL simulations to take into account the antenna design, capacitive coupling, glass substrate and placement within the large array. The losses in the resistive Titanium Nitride in turn heat up the attached amorphous silicon layer. Separating the bulk of the antenna from the heat sensing component allows the pixel to have a fast and sensitive thermal response.

Not shown in Figure 4b are the mechanical hinges that suspend the resistor above the antenna layer with the gap controlled by designing the appropriate sacrificial layer thicknesses. A reflective mirror surface must be provided one quarter wavelength away from the antenna to maximize the coupling with the incident radiation. Although conventional bolometric structures not involving antennas are straightforward, with the absorber and sensor maximally filling each pixel area, the resulting thermal capacitance would be huge due to the large spatial scales involved and would thus result in an excessively slow response. A properly designed antenna can project an effective fill factor for each pixel that approaches unity as demonstrated in the COMSOL simulations shown in Figure 6. The simulations utilize Floquet-periodic boundary conditions on four sides of the unit cell to simulate an infinite 2-D array [37]

We chose a crossed dipole antenna configuration to eliminate any dependence on the polarization of the incident radiation. As shown in Figure 5, the 0.7mm pixel was divided into a 2x2 array of subpixels with each having an identical pair of crossed dipoles. The resistive loads are electrically connected in parallel, from a readout perspective. The antennas (tan color) are fabricated on the glass substrate while the blue structures are suspended over the antenna with the sensor capacitively coupled to the antenna. The blades of the dipole are broadened at the ends to widen the frequency response.

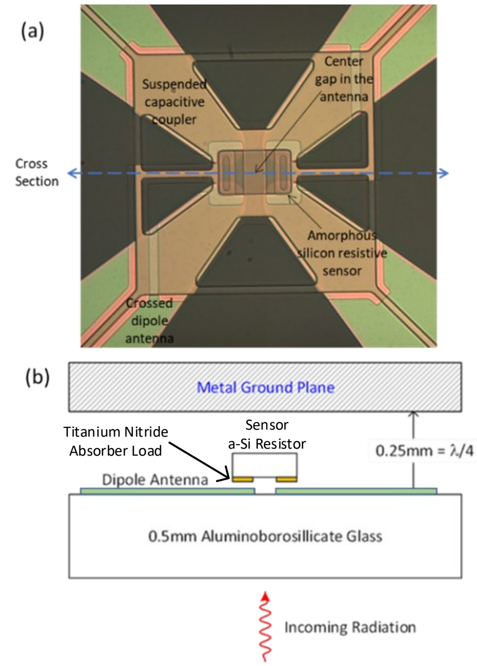

Fig. 4. Antenna Coupled Bolometer (a) close up of the capacitively coupled center resistor (b) cross section

The initial antenna design consisted of one constituent crossed dipole as shown in Figure 6a where the dipole antenna is continuous with no gaps at the center. The S_{11} reflection was calculated using COMSOL as a function of frequency, as shown in Figure 6b. Note that the reflection of the antenna alone on the glass substrate (perfectly conducting dipoles shorted at the center hence without the capacitive gap) reaches its peak at a frequency of about 220 GHz which is lower than the targeted design frequency.

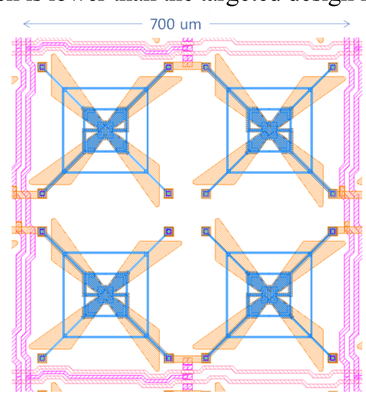

Fig. 5. Pixel Layout comprising a 2x2 array of subpixels

With the inclusion of the capacitively-coupled component as needed in the actual pixel operation, the center frequency increases. This strong antenna resonance is capacitively coupled to the suspended resistive load as shown in Figure 7a. The simulations indicated that the capacitive overlap of the load, geometrically about 25% of the antenna length, is sufficient to provide over 90% of absorption by resistive losses for a bandwidth of over 30% as shown in Figure 7c-d. A quarter wave away from the glass surface, a high reflectance mirror creates a “quarter wave back short” to enhance absorption at the resistive load by constructing an antinode at that plane.

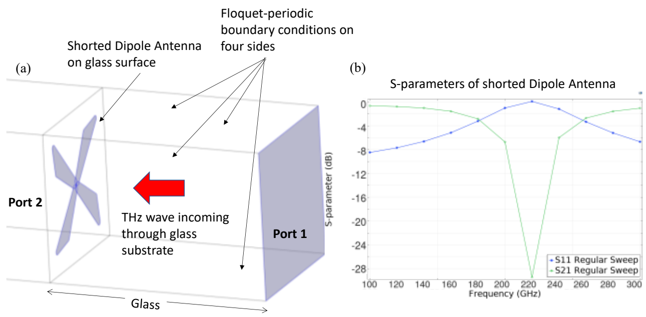

Fig. 6. (a) Crossed dipole antenna on the glass substrate, (b) S_{11} and S_{21} from and through antenna plane

TABLE 1 Design Parameters for THz Pixel Array

Parameter	Value	Note
Antenna array pitch (subpixel)	350 um	Each imaging pixel consists of a 2x2 subarray of antennas resulting in 700um pixel pitch
Dipole length (each)	400 um	Two crossed dipoles for polarization insensitivity
Gap at center of dipole	13 um	Electrical gap at the center of dipole to direct coupling to suspended absorber plate.
Hinge length (each of the 4)	125 um	
Hinge width	1.5 um	
Hinge thickness	100 nm	Comprised of a trilayer stack of Silicon Nitride-Titanium Nitride-Silicon Nitride
Thermal conductance (total from 4 hinges)	1.4e-8 W/K	Material thermal conductivity is approximately 2 W/m K
Hinge stress	300 MPa	To provide the stiffness to suspend the absorber
Capacitive gap	3 um	Absorber is suspended above the metal antenna on the glass substrate
Capacitor area	4000um^2	
Capacitance value	12 fF	Coupling capacitance between antenna and center load of each subpixel
Sensor TCR	2.5% /°K	TCR of amorphous silicon
a-Si sensor volume	29 um x 18 um x 250 nm	

To maximize the absorption at the desired band, the antenna length and shape, capacitive gap, resistive load, pixel pitch and quarter-wave mirror spacing need to be optimized simultaneously. These simulations (Figures 7c-d) show how the absorption spectrum varies with the capacitive gap and overlap area. The design is fairly tolerant to capacitive gap and area to achieve absorption exceeding 10 dB as shown in the figures below where the capacitive gap is varied from 2 um to 10 um, and the capacitive overlap area is varied from 10 to 35% of the antenna area. At the 35% capacitive overlap, the peak wavelength is detuned enough to be mismatched to the quarter wave cavity resonance resulting in slightly lower absorption.

Since the peak absorption frequency depends on the capacitance of the suspended load as shown in Figure 7c-d, the length of the antenna on the glass must be tuned appropriately for a given choice of parameters. The design values in Table 1 correspond to a peak absorption around 300 GHz.

Due to the thermal isolation enabled by the long, thin, and narrow hinges , the resistive losses in the suspended load cause the temperature of the amorphous silicon sensor to rise. The temperature change causes the resistance of the amorphous silicon to change which is then detected by the Palomar ROIC through the LTPS switching backplane. Table 2 shows the thermomechanical design parameters of the pixel.

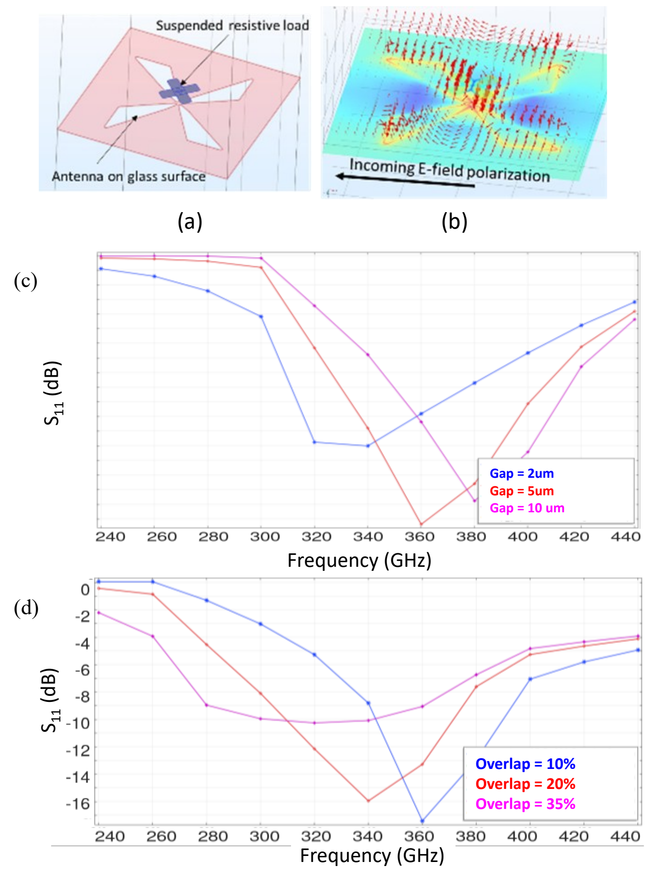

Fig. 7. (a) Suspended resistive load capacitively coupled to the antenna below, (b) E-field visualization on the plane of the antenna on the glass substrate at resonance, (c) Reflection (S_{11}) from the resistively loaded antenna showing tolerance to gap changes, (d) S_{11} tolerance with area changes. Peak absorption frequency decreases with increases in capacitive coupling.

The hinges are designed with high tensile stress to pull the suspended structure flat like a rubber band in tension. It comprises a conductive middle layer sandwiched by an insulating dielectric to provide high tensile stress. The cross bracing reduces sensitivity to tilting. The heterogenous center stack of the resistive load and the silicon sensor built on top of the hinge layers will have different stresses which can cause the center of the suspended region to curl down slightly.

Figure 8a shows the mechanical simulation of the structure that matches the 3D Laser Scanning Microscope (Olympus OLS4000) image of a fabricated device shown in Figure 8b. The stresses in the center layers cause the center of the pixel to rise above the plane of the sacrificial layer upon release. This result comes from a single fabrication run that was not completely optimized, as evidenced from film stress that caused the center portion of the pixel to be touching down to the substrate, thereby causing the effective hinge length to be shorter than designed. A thin dielectric with tensile stress deposited on the top will correct for this curling due to stress gradient. When the film properties are thus optimized, the thermal conductance should meet the design target of 1.4e-8 W/K instead of much larger value of 1e-5 W/K that we estimate based on where the pixel makes contact with the substrate.

With the ROIC dynamic range set to 40% of the bias current of each channel, the ADC has at least 12 bits of resolution. Thus the minimum detectable change of resistance is $\frac{40}{100}/2^{12} = 100\,ppm.$ Given an amorphous silicon resistor with Temperature Coefficient of Resistance (TCR) of 2.5%/K, the minimum detectable temperature change is $\frac{100\,ppm}{0.025} = 4\,mK.$ With the thermal isolation as designed in Table 1, the Minimum Detectable Power (MDP) is $1.4 \times 10^{-8} W/K \times 4mK = 56$ pW per pixel. Since the pixel is not fully suspended, the estimated thermal isolation is over 1e-5 W/K resulting in an MDP of 40-100 nW.

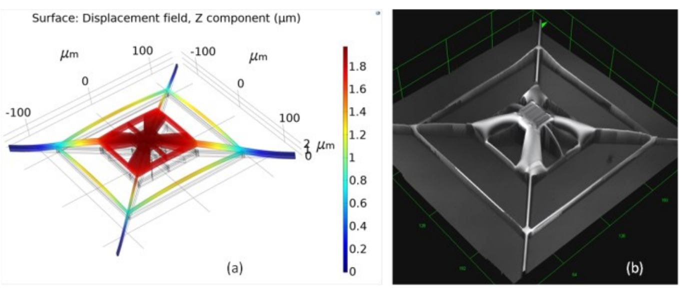

Fig. 8 (a) Mechanical simulation of the suspended structure, (b) 3D Laser Scanning Microscope image of the fabricated device.

III. Sigma Delta ROIC for THz Array

The Obsidian THz image sensor requires a custom read-out system, capable of sensing small changes in pixel currents with sufficient precision and signal-to-noise ratio for the applications discussed above. To this end, Obsidian has developed the Palomar custom Read-Out Integrated Circuit (ROIC) using a mixed-signal 180nm CMOS technology with HV capability.

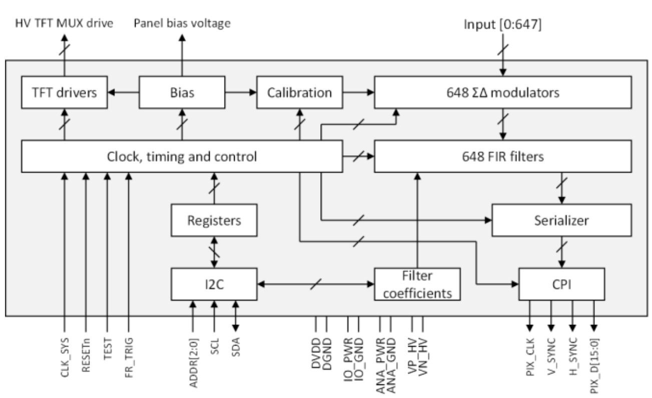

Fig. 9. Palomar ROIC Block Diagram

The main functional blocks of the ROIC are illustrated in Figure 9. The input from each array column is passed to a data path including a current-sensing analog-to-digital converter (comprised of a second-order sigma-delta modulator and programmable FIR filter), a data serializer and finally the digital output via a CPI interface. A bias block provides all required internal bias and reference signals as well as the bias voltage for the sensor array; no external reference is required. An on-chip calibration block generates signals required for both self-test and in-situ chip calibration. High voltage TFT drivers are also provided to control the on-glass TFT row select circuits.

Figure 10 illustrates the panel bias drive and pixel sensing using the Palomar ROIC. The panel bias voltage generator is designed such that the quiescent pixel current is I_{BIAS}, and the difference between I_{BIAS} and the actual pixel current in the presence of radiation incident on the sensor array is passed to the ADC.

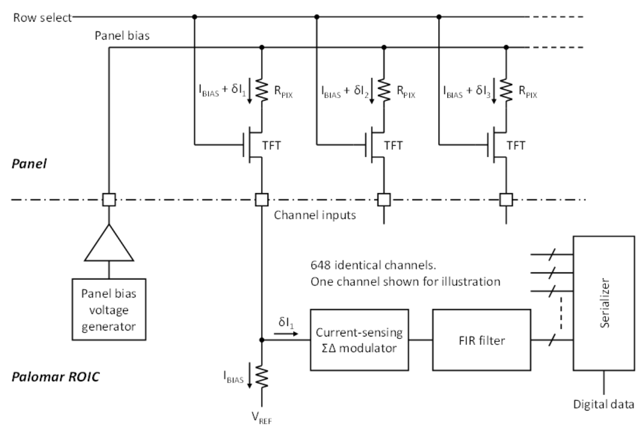

Fig. 10. Palomar panel drive and pixel drive sensing

The chip is fully programmable and can accommodate different sensor panel sizes, frame rates, and system timing. The ADCs can be programmed to match different pixel modes and characteristics, with adjustable bias current and range, programmable over-sampling ratio (OSR) and filter coefficients.

Achieving a high signal-to-noise ratio in the ADCs is critical. In order to do this, the Palomar chip design includes measures to suppress internal sources of noise (MOSFET 1/f noise, switching noise, power supply and reference voltage ripple etc.). The success of these measures is demonstrated by the fact that the measured ADC SNR is determined primarily by thermal resistor noise at the ADC input.

Figure 11 shows typical ADC equivalent number of bits (ENOB) measured for 3 randomly selected ICs from a wafer, calculated from the SNR according to IEEE Standard 1241-2010, "IEEE Standard for Terminology and Test Methods for Analog-to-Digital Converters", Section 9.4 [38]. The data are plotted as functions of the OSR, and for values above about 120, the results correspond to a fixed input referred noise that closely matches the calculated thermal noise arising from the panel and on-chip resistors connected to the ADC input. The increase in ENOB for higher values of OSR simply arises from the reduced equivalent noise bandwidth as the conversion time increases with higher OSR. With an OSR of around 240, an ENOB of about 11.5 is achieved; with an OSR of 1000, the ENOB increases to about 12.5.

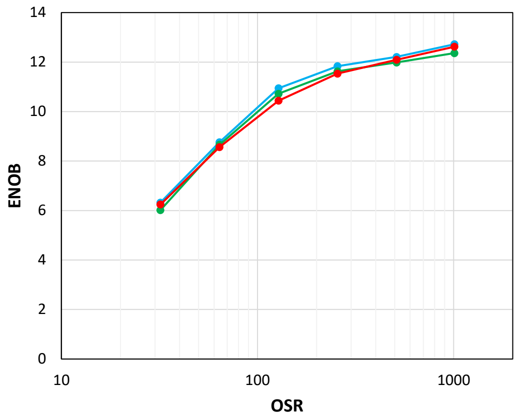

Fig. 11. Palomar ADC ENOB (3 sample chips)

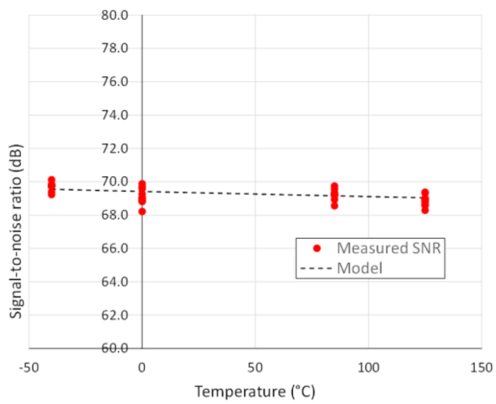

Fig. 12. Palomar ADC SNR and temperature (OSR=240)

Figure 12 shows the typical ADC SNR as a function of temperature, and it is clear that the ADC performance is maintained across a wide operating temperature range (-40°C to 105°C). The SNR values are slightly lower than those shown in Figure 12 due to some residual interference from the environmental test system. Nevertheless, the expected small decrease in SNR due to increased thermal noise generated in the input resistors as temperature rises can be seen. The modeled curve shown on the plot is simply based on the calculated thermal noise and matches the measured data well.

TABLE 2
SELECTED PALOMAR ROIC CHARACTERISTICS

Characteristic	Typical Value	Comments
Power	< 1mW/channel	Full chip power dissipation
TFT drive signal swing	-5V to +15V	
ADC ENOB	>11 (OSR=240) >12 (OSR=1000)	Limited by input resistor thermal noise
ADC linearity	INL≈0.04% of full scale	
ADC non-uniformity	≈2% of full scale, uncorrected <0.1% of full scale, corrected	Non-uniformity correction based on simple two-point method

Table 2 summarizes some additional Palomar chip characteristics. Of particular note are the low power per channel (<1mW, accounting for the power from all chip blocks including the digital sections, bias generation and TFT drivers) and the excellent uniformity.

IV. DEMONSTRATION

The system demonstration set up is illustrated in Figure 13 with the electrical subsystem (pixel panel, ROIC and controller PCB) described in Figure 14. A multiplier source nominally set at 300GHz was used, purchased from Virginia Diodes. The waveguide horn output was directed to the THz array which was placed in an evacuated chamber with a 10mm thick THz window made with the transmissive material TPX (Polymethylpentene) [39, 40]. TPX absorption at 300GHz is known to be extremely low and we estimate that the loss through the window is less than 10% including the Fresnel reflection losses.

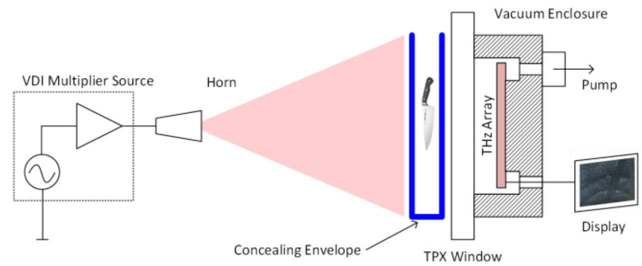

Fig. 13. THz Demonstration System

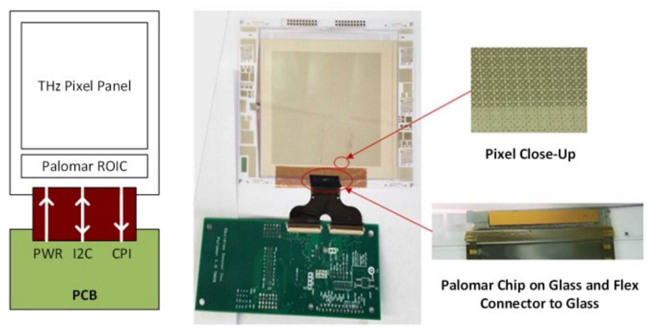

Fig. 14. THz Electrical Subsystem

A metallic knife was placed inside a cardboard envelope and the radiation transmitted through the envelope was captured by the THz array. The metallic knife produced an occlusion shadow (and diffraction patterns around the blade), as evident in the video frames captured in Figure 15 (captured by a cellphone camera viewing the computer display). The circular arcs in the THz image are from interference fringes produced by the parallel surfaces of the window material. Note that the diffraction patterns due to the knife edges are visible. As mentioned earlier, the microbolometer structures in this device were partially collapsed due to the unbalanced stresses in the mechanical hinge layers. The partial collapse in turn greatly increased the thermal conductance, decreasing the thermal transduction gain. Using the estimated thermal conductance of the partially suspended pixels, the MDP is estimated to be 100 nW as calculated previous. Lastly, as the Palomar chip was not ready at the time of the demonstration experiment, a set of 5 ADCs (National Instruments PCIe-6363) on a PCB was used to readout the array. With the sampling time set at 100usec, the array was read out at a frame rate of 3 Hz considerably lower than what is possible with the Palomar ASIC (each ADC was used to read out 26 columns with a dwell time of 100usec for each row leading to a total read time of 128 X 26 X 100usec = 330msec).

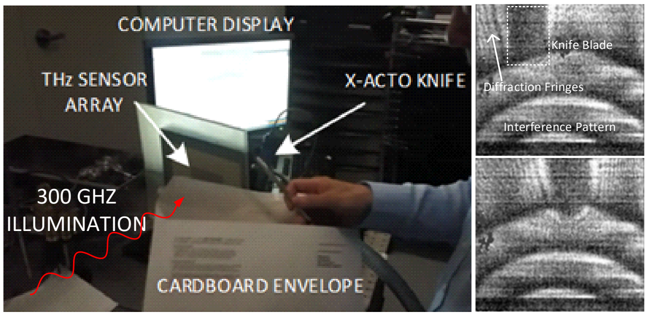

Fig. 15. Demonstration example (upper photo shows the illumination direction, the envelope containing the knife, the TPX cover and the sensor array; lower photos show two frames from the 3fps video with the knife entering from the top portion of the image)

TABLE 3 Comparisons of Staring THz Sensor Arrays

Sensor Technology	**Frequency**	**Array size and pitch**	**Nyquist sampling pitch at F/1**	**Sensitivity per pixel**	**Frame rate**
Patch Antenna-CMOS [33]	900 GHz	32 x 32 @ 215 um	167 um	NEP 91 pW/$\sqrt{Hz}$	400 fps
GaAs plasmonic detector [34]	50-700 GHz	64 x 64 @ 1.5 mm	3 mm to 220 um	NEP 1 nW/$\sqrt{Hz}$	1 fps
Antenna-coupled microbolometer [35]	1.7 and 2.5 THz	320 x 240 @ 50 um	88 to 60 um	68 pW (1.7 THz) 32 pw (2.5 THz)	
Ring Antenna-CMOS [36]	790-960 GHz	32 x 32 @ 80 um	289 to 156 um	NEP 100 pW/$\sqrt{Hz}$	500 fps
Microbolometer [30]	300-4280 GHz	640 x 480 @ 23.5 um	500 to 35 um	MDP 6 nW (at 300 GHz) to 20 pW (at 4.3 THz)	30 fps
Bowtie-CMOS [41]	270, 600 GHz	31 x 31 @ 240 um	560, 250 um	MDP 0.6 nW (at 270 GHz) to 0.8 nW (at 600 GHz)	100 fps
Patch Antenna-CMOS	300 GHz	7x7 @ 500 um	500 um	NEP 20 pW/$\sqrt{Hz}$	
Antenna-coupled microbolometer [this work]	300 GHz	128 x 128 @ 700 um	500 um	MDP 60 pW (as designed), 100 nW measured	100 fps (with ROIC)

NEP = Noise Equivalent Power
MDP = Minimum Detectable Power

V. Summary

A new terahertz imaging sensor array was described, using a unique MEMS on glass manufacturing technology. The antenna-coupled microbolometer sensor module that was presented achieves a 128x128 pixel resolution at the Nyquist spatial sampling rate but can be scaled up to much higher resolutions that are called for in important medical and security applications. Key components of the sensor module including the design and demonstration of the readout integrated circuit (ROIC) were described. The design and build of complete camera systems including appropriate lenses will be reported in a future publication.

ACKNOWLEDGEMENT

This material is based upon work supported by the National Science Foundation under Grant No. 2013992

References

[1] D. Pavlidis, D., “Fundamentals of Terahertz Devices and Applications,” John Wiley & Sons, 2021.
[2] T. Nagatsuma, “Terahertz technologies: present and future,” IEICE Electronics Express, Vol. 8, No.14, pp. 1127-1142, 2011.
[3] C. Jansen, S. Wietzke, O. Peters, M. Scheller, N. Vieweg, M. Salhi, N. Krumbholz, C. Jördens, T. Hochrein, and M. Koch. "Terahertz imaging: applications and perspectives," Applied Optics Vol. 49, No. 19, E48-E57 , 2010.
[4] D. Arnone, C. Ciesla, and M. Pepper,"Terahertz imaging comes into view," Physics World Vol. 13, No. 4, 2000.
[5] W. L. Chan, J. Deibel, and D. M. Mittleman, "Imaging with terahertz radiation." Reports on progress in physics 70, No. 8, 2007.
[6] C. Yu, S. Fan, Y. Sun, and E. Pickwell-MacPherson, "The potential of terahertz imaging for cancer diagnosis: A review of investigations to date," Quantitative imaging in medicine and surgery Vol. 2, No. 1, 2012.
[7] B. B. Hu, and M. C. Nuss, "Imaging with terahertz waves," Optics Letters 20, No. 16, pp. 1716-1718, 1995.
[8] J. A. Zeitler and Y. C. Shen, "Industrial applications of terahertz imaging." In Terahertz Spectroscopy and Imaging, pp. 451-489, Springer, Berlin, Heidelberg, 2012.
[9] K. Ahi, Kiarash, N. Asadizanjani, S. Shahbazmohamadi, M. Tehranipoor, and M. Anwar, "Terahertz characterization of electronic components and comparison of terahertz imaging with x-ray imaging techniques." In Terahertz Physics, Devices, and Systems IX: Advanced Applications in Industry and Defense, Vol. 9483, p. 94830K. International Society for Optics and Photonics, 2015.
[10]J. B. Jackson, M. Mourou, J. F. Whitaker, I. N. Duling Iii, S. L. Williamson, M. Menu, and G. A. Mourou. "Terahertz imaging for non-destructive evaluation of mural paintings." Optics communications 281, No. 4, pp. 527-532, 2008.
[11]A. W. M. Lee, Q. Qin, S. Kumar, B. S. Williams, Q. Hu, and J. L. Reno, "Real-time terahertz imaging over a standoff distance (> 25 meters)," Applied Physics Letters 89, No. 14, p.141125, 2006.
[12]M. Lu, J. Shen, N. Li, Y. Zhang, C. Zhang, L. Liang, and X. Xu, "Detection and identification of illicit drugs using terahertz imaging," Journal of Applied Physics 100, No. 10, p.103104, 2006.
[13]P. H. Siegel, “Terahertz technology,” IEEE Transactions on Microwave Theory and Techniques, 50, No. 3, pp.910-928, 2002.
[14]D. M. Mittleman, “Perspective: Terahertz science and technology,” Journal of Applied Physics, 122, No. 23, p.230901, 2017.
[15]M. A. Butavicius, K. M. Parsons, A. McCormac, R. Foster, A. Whittenbury, and V. MacLeod, “Assessment of the ThruVision T4000 Passive Terahertz Camera: A Human Factors Case Study.” In Innovations in Defence Support Systems-2, pp. 183-206, Springer, Berlin, Heidelberg, 2011..
[16]M. Kowalski, M. Kastek, M.Piszczek, M. Życzkowski, and M. Szustakowski, “Harmless screening of humans for the detection of concealed objects.” Safety and Security Engineering VI, 151, pp.215-223,2015.

[17]C. Mann, “First demonstration of a vehicle mounted 250GHz real time passive imager,” Proc. SPIE 7311, Terahertz Physics, Devices, and Systems III: Advanced Applications in Industry and Defense, 73110Q April, 2009.
[18]K. B. Cooper, R. J. Dengler, N. Llombart, B. Thomas, G. Chattopadhyay, and P. H. Siegel, "THz imaging radar for standoff personnel screening," IEEE Transactions on Terahertz Science and Technology 1, No. 1, pp. 169-182, 2011.
[19]F. Ellrich, M. Bauer, N. Schreiner, A. Keil, T. Pfeiffer, J. Klier, S. Weber, J. Jonuscheit, F. Friederich, and D. Molter, "Terahertz quality inspection for automotive and aviation industries," Journal of Infrared, Millimeter, and Terahertz Waves 41, No. 4, pp.470-489, 2020.
[20]G. C. Walker, E. Berry, S. W. Smye, D. S. Brettle, “Materials for phantoms for terahertz pulsed imaging,” Physics in Medicine and Biology, Vol. 49, pp N363-N369, 2004.
[21]A. J. Fitzgerald, E. Berry, N. N. Zinovev, S. Homer-Vanniasinkam, R. E. Miles, J. M. Chamberlain, and M. A. Smith, “Catalogue of Human Tissue Optical Properties at Terahertz Frequencies,” Journal of Biological Physics, Vol. 29, pp 123-128, 2003.
[22]P. C. Ashworth, E. Pickwell-MacPherson, E. Provenzano, S. E. Pinder, A. D. Purushotham, M. Pepper, and V. P. Wallace, “Terahertz pulsed spectroscopy of freshly excised human breast cancer,” Optics express, Vol. 17, No. 15, pp.12444-12454, 2009.
[23]D. D. Arnone, C. M. Ciesla, A. Corchia, S. Egusa, M. Pepper, J. M. Chamberlain, C. Bezant, E. H. Linfield, R. Clothier, and N. Khammo. "Applications of terahertz (THz) technology to medical imaging," In Terahertz Spectroscopy and Applications II, Vol. 3828, pp. 209-219, International Society for Optics and Photonics, 1999.
[24]Z. D. Taylor, S. Singh, M. O. Culjat, J. Y. Suen, W. S. Grundfest, H. Lee, and E. R. Brown. "Reflective terahertz imaging of porcine skin burns," Optics Letters 33, No. 11, pp. 1258-1260, 2008.
[25]Z. D. Taylor, R. S. Singh, D. B. Bennett, P. Tewari, C. P. Kealey, N. Bajwa, M. O. Culjat, "THz medical imaging: in vivo hydration sensing," IEEE Ttransactions on Terahertz Science and Technology 1, no. 1 (2011): 201-219.
[26]Y.B. Ji, S.J. Oh, S.G. Kang, J. Heo, S.H. Kim, Y. Choi, S. Song, H. Y. Son, S. H. Kim, J. H. Lee, and S. J. Haam, “Terahertz reflectometry imaging for low and high grade gliomas,” Scientific Reports, 6, p.36040, 2016.
[27]W. Stummer, A. Novotny, H. Stepp, C. Goetz, K. Bise, and H. J. Reulen, "Fluorescence-guided resection of glioblastoma multiforme utilizing 5-ALA-induced porphyrins: a prospective study in 52 consecutive patients," Journal of neurosurgery 93, No. 6, pp. 1003-1013, 2000.
[28]S. H. Choi, Y. Changhwan, and M. Kim. "A 269-278 GHz voltage-controlled oscillator with uniform output power of 5 dBm," Microwave and Optical Technology Letters 61, No.4, pp.959-962, 2019.
[29]J. Suszek, A. M. Siemion, N. Blocki, M. Makowski, A. Czerwinski, J. Bomaba, A. Kowalczyk, I. Ducin, K. Kakarenko, N. Palka, P. Zagrajek, M. Kowalski, E. Czerwinska, C. Jastrzebski, K. Switkowski, J. L. Coutaz, A. Kolodziejczyk, and M. Sypek, "High order kinoforms as a broadband achromatic diffractive optics for terahertz beams." Optics Express 22, No.3, pp. 3137-3144, 2014.
[30]N. Oda, M. Sano, K. Sonoda, H. Yoneyama, S. Kurashina, M. Miyoshi, T. Sasaki, I. Hosako, N. Sekine, T. Sudou, and S. Ohkubo, "Development of terahertz focal plane arrays and handy camera," In Infrared Technology And Applications XXXVII, Vol. 8012, p. 80121B, International Society for Optics and Photonics, 2011.
[31]H. Spisser, S. Ouellet, C. Vachon, M. Terroux, M. Briand, F. Berthiaume, M. Doucet, A. Paquet, H. Oulachgar, F. Genereux, L. Marchese, "Terahertz imaging of large objects with high resolution." In Millimetre Wave and Terahertz Sensors and Technology XIII, Vol. 11541, p.1154106, International Society for Optics and Photonics, 2020.
[32]N. Oda, “Uncooled bolometer-type terahertz focal plane array and camera for real-time imaging,” C. R. Physique 11 (2010).
[33]S. Yokoyama et al., "5.8 A 32×32-Pixel 0.9THz Imager with Pixel-Parallel 12b VCO-Based ADC in 0.18μm CMOS," 2019 IEEE International Solid-State Circuits Conference - (ISSCC), 2019, pp. 108-110.
[34]https//terasense.com/products/sub-thz-imaging-cameras/
[35]F. Simoens, J. Meilhan, L. Dussopt, J. A. Nicolas, N. Monnier, G. Sicard, A. Siligaris, and B. Hiberty. "Uncooled Terahertz real-time imaging 2D arrays developed at LETI: present status and perspectives," In Micro-and Nanotechnology Sensors, Systems, and Applications IX, Vol. 10194, International Society for Optics and Photonics, 2017.
[36]A. Hadi, R., Sherry, H., Grzyb, J., Zhao, Y., Forster, W., Keller, H. M., ... and Pfeiffer, U. R. (2012). A 1 k-pixel video camera for 0.7–1.1 terahertz imaging applications in 65-nm CMOS. IEEE Journal of Solid-State Circuits, 47(12), 2999-3012.
[37]https://www.comsol.com/model/frequency-selective-surface-periodic-complementary-split-ring-resonator-15711
[38]S. Rapuano, J. Jendzurski, L. De Vito, S. J. Tilden, W. B. Boyer, and N. G. Paulter, "The documentary standards of the IEEE technical committee 10," IEEE Instrumentation & Measurement Magazine 23, No. 8, pp.8-13, 2020.
[39]L. C. Lopez, G. L. Wilkes, P. M. Stricklen, and S. A. White, "Synthesis, structure, and properties of poly (4-methyl-1-pentene)," Journal of Macromolecular Science, Part C: Polymer Reviews 32, No. 3-4, pp.301-406, 1992.
[40]M. Naftaly, R. E. Miles, and P. J. Greenslade, “THz transmission in polymer materials—a data library,” 2007 Joint 32nd International Conference on Infrared and Millimeter Waves and the 15th International Conference on Terahertz Electronics (pp. 819-820). IEEE.
[41]A. Boukhayma, A. Dupret, JP. Rostaing, and C. Enz, “A low-noise CMOS THz imager based on source modulation and in-pixel high-Q passive switched-capacitor N-path filter,” Sensors 2016, 16(3):E325
[42]K. Song, J. Kim, D. Kim, MG. Seo, JS. Rieh, “A CMOS 300-GHz 7 by 7 detector array for THz imaging,” 2017 IEEE International Symposium on Radio-Frequency Integration Technology (RFIT), 2017, pp. 31-33

John Hong (Senior Member, IEEE) John Hong received the B.S. degree from Massachusetts Institute of Technology, Cambridge, Massachusetts and the Ph.D. degree from California Institute of Technology, all in electrical engineering. He has had technology development and management roles at Rockwell, Acelo Semiconductor, Jet Propulsion Laboratory and Qualcomm. He is currently the CEO of Obsidian Sensors in San Diego, CA and also an adjunct professor at UCSD ECE Department in La Jolla, CA. He is a fellow of the Optical Society of America and has served as a Topical Editor of the journal Optics Letters.

Sean Andrews graduated with distinction with B. S. Degrees in Chemistry and Mathematics from the University of Wisconsin – Madison. He received his Ph.D. in chemistry from University of California – Berkeley, developing novel nanostructured inorganic materials for thermoelectric energy conversion and membranes in SOFCs. He is a principal scientist at Obsidian Sensors working on material science, process engineering and device. Before joining Obsidian Sensors in 2018, Sean was a staff scientist in Corporate R&D at Qualcomm researching thermal mitigation solutions for advanced node technologies and on-chip power systems. Sean has authored over 20 peer-reviewed publications and has been recognized with several research awards, as well as UC – Berkeley's 'Nanoscale Science & Engineering Distinguished Service Award' in 2012 for his work in nanowire thermal transport.

Jan Bos studied theoretical physics at the Free University in Amsterdam and received his Ph.D. degree in nuclear physics from the University of Amsterdam in 1993. After a three years postdoc term at the Academia Sinica in Taipei he worked at Picvue Electronics, a LCD manufacturer also in Taiwan, as adjunct VP of Operations till 2004. There he held a board position at start-up MEMS display company Iridigm which he joined as engineering director later. From 2005 till 2016 he was senior director of engineering at Qualcomm Taiwan and he currently serves Obsidian Sensors Taiwan as country manager.

Edward Chan received the B.S degree in 1994, and the Ph.D. degree in 2000 from Stanford University, all in electrical engineering. From 2000 until 2010, he developed optical and wireless components at Bell Labs, Murray Hill, optimized the signal integrity and packaging of Intel and Nvidia microprocessors, and engineered tunable liquid crystal components at DigiLens. From 2010 to 2017, he was the Director of Engineering with Qualcomm Research, San Diego, where he designed continuously tunable reflective MEMS displays and wireless power systems. He is currently the Senior Director of Engineering at Obsidian Sensors in San Diego.

Tallis Chang received the B.S. degree in electrical engineering and computer science from University of California at Berkeley in 1979, and the M.S. and Ph.D. degrees in electrical engineering from the University of Southern California in 1981 and 1986, respectively. He co-founded Obsidian Sensors and is currently the COO of the company. From 2009 to 2017, he was a senior director of engineering at Qualcomm, leading an engineering team to develop the next-generation MEMS reflective displays. He has over 30 years of technical and management experience, developing optical and MEMS devices and systems for commercial, space, and military applications with technology development and management roles at Rockwell Science Center, Jet Propulsion Laboratory, Chromux Technologies, Panavision Federal Systems, and Qualcomm. He has over 100 journal articles and conference publications and holds 29 U.S. patents.

Vincent Condito (Senior Member IEEE) received the B.S. degree in electrical engineering from Massachusetts Institute of Technology, Cambridge, Massachusetts in 1976 and has done graduate work at Stanford University, Palo Alto, California.
He has worked on a wide variety of integrated circuit design projects across the industry including Hewlett-Packard, Analog Devices, Micro Linear, Fairchild, Exar, Big Bear Networks, Qualcomm, Alterra, Sandisk, Panasonic, Infinera, Microsemi, Maxim, Pericom.

Alan Lewis (Fellow IEEE) received the MA degree in physics from the University of Oxford, UK. His professional work has included CMOS process development and integration, mixed signal IC design, large area electronics, display system development, solid state lasers and chip-level security systems. He has served on various conference organizing committees including IEDM, ISSCC, SID and IDRC.

Murilo Pessatti (Member, IEEE) received received the B.S. degree from São Paulo University, São Paulo, Brazil, and the M.S. from the State University of Campinas, Brazil, all in electrical engineering with focus in Analog IC Design. He worked for Chipidea (acquired by Synopsys) in the power management IC design group. He founded Chipus Microeletrônica S.A. in 2008, where he is currently CEO and Chief of the BOD. He is also Innovation Director for the Brazilian Semiconductor Association (ABISEMI).

Seung Tak Ryu (Senior Member, IEEE) received the B.S. degree in electrical engineering from Kyungpook National University, Daegu, South Korea, in 1997, and the M.S. and Ph.D. degrees from the Korea Advanced Institute of Science and Technology (KAIST), Daejeon, South Korea, in 1999 and 2004, respectively.
From 2001 to 2002, he was a Visiting Researcher with the University of California at San Diego, La Jolla, CA. In 2004, he joined Samsung Electronics, Yongin, South Korea. From 2007 to 2009, he was an Assistant Professor with Information and Communications University (ICU), Daejeon. He has been with the Department of Electrical Engineering, KAIST, since 2009, where he is currently an Associate Professor.
Prof. Ryu has served on the Technical Program Committee (TPC) for the IEEE International Solid-State Circuits Conference (ISSCC). He has served as a Guest Editor for the IEEE JOURNAL OF SOLID-STATE CIRCUITS (JSSC) twice. He has been an Associate Editor of IEEE SOLID-STATE CIRCUITS LETTERS (SSCL) since 2018 and the IEIE Journal of Semiconductor Technology and Science (JSTS) since 2020.

Heesun Shin received the B.S. and Ph.D. degrees from Seoul National University, in electrical engineering, in 2003 and 2009 respectively. He is a senior staff engineer responsible for designing and validating LTPS thin film transistor (TFT) circuits at Obsidian Sensors. He has over 11 years of experience in designing TFT circuits and manufacturing process engineering for on-glass devices. From 2015 to 2917, he was a staff engineer at Qualcomm working on MEMS reflective displays. From 2009 to 2014, he worked at LG Display developing small display products and touch sensors, where he received several awards for new product introduction and innovation. He has 40 journal papers and 41 patents in US and Korea.

Bing Wen received the B.S. degree in Physics at Tsinghua University in Beijing in 1993 and Ph.D. in physics at Case Western Reserve University in 2003, where he studied the electro-optical properties of liquid crystals. He is a director of engineering at Obsidian Sensors, leading the device/system characterization efforts. From 2011 to 2017, he was a principal engineer at Qualcomm developing MEMS based reflective displays, and, from 2003 to 2011, he was a member of the technical staff at Rockwell Scientific Company (which later became Teledyne Scientific) developing a wide range of novel devices, including beam steering, wave front shaping, motion tracking, and special purpose cameras. He as 20 publications and 20 US patents in related areas.